A semi-phenomenological spherical optical model potential for elastic scattering of nucleons up to 200 MeV.

E. Bauge, J.P. Delaroche, J. Dechargé, M. Girod

Service de Physique Nucléaire
Centre d'Études de Bruyères-le-Châtel
BP 12, 91680 Bruyères-le-Châtel, France

Abstract

In this work we present a semi-phenomenological spherical optical model potential (OMP), for elastic scattering of incoming neutrons or protons on A$\geq$40 nuclei, up to 200 MeV. The central part of this OMP is formally identical to that derived by Jeukene, Lejeune and Mahaux (JLM) from Brückner-Hartree-Fock calculations in nuclear matter. However, discontinuities in the parametrisations of the imaginary part of the JLM OMP at 10 MeV, and the pathology exhibited by the imaginary part of this OMP when extrapolated above 160 MeV, led us to re-fit the imaginary part of the JLM nuclear matter potential. For the spin-orbit (SO) potential, we use a phenomenological complex SO potential with a Scheerbaum form factor, permitting us to get good fits to the experimental differential cross sections and analyzing powers, up to 185 MeV. We then allow the normalizations of the potentials depths to vary as a function of energy in order to get the best fit to experimental elastic scattering data, and we express these variations with a functional form, thus getting a global OMP for nucleons up to 200 MeV. This global OMP, built using point proton and neutron radial densities calculated in the Hartree-Fock-Bogoliubov (HFB) framework with the Gogny force, is able to account fairly well for the experimental angular distributions and reaction cross sections, provided the target nucleus is spherical (i.e., ^{40}Ca, ^{90}Zr, ^{93}Nb, ^{116}Sn, ^{120}Sn, ^{208}Pb, ^{209}Bi) or quasi-spherical (i.e., ^{54}Fe, ^{56}Fe, ^{58}Ni, ^{60}Ni, ^{63}Cu, ^{65}Cu).

1 Introduction.

The construction of a microscopic optical model potential(OMP) is a necessary step if one is to predict elastic scattering and reaction cross sections without having to rely upon measurements. This step has been taken with the construction of microscopic OMPs [1, 2] that have been used successfully in experimental data analysis [3, 4, 5, 6, 7]. However, for most of these studies, [3] being a notable exception, the OMP used was only microscopic in the sense of being formally derived from a realistic bare nucleon-nucleon interaction, while the point proton and neutron radial densities used in the calculation were derived from experimental measurements. In this study we take the further step, pioneered in [3], of using theoretically calculated nucleon densities for the calculation of the OMP, thus removing the need for experimental nucleon densities. Moreover, in order to account for experimental data at energies up to 200 MeV, the central part of the OMP must be supplemented with a good quality spin-orbit (SO) potential. Lastly, while the microscopic OMP gives good qualitative agreement with experimental data without any phenomenological adjustments, such adjustments are needed if one is to get a more quantitative agreement [4].

So, in this work we used the microscopic JLM OMP [1], with HFB nucleon densities. Due to energy limitations of the original JLM OMP, the imaginary part of the interaction was re-fitted in the 0 to 200 MeV energy range, giving a new parametrisation of the absorption part of the interaction of nucleons within nuclear matter. The use of a complex SO potential with the Scheerbaum form factor [8], along with global parametrisations of phenomenological normalizations, based on our systematic study , leads to predicted observables which closely track the experimental data. The calculations are performed using the codes FLIT [9] and ECIS95 [10].
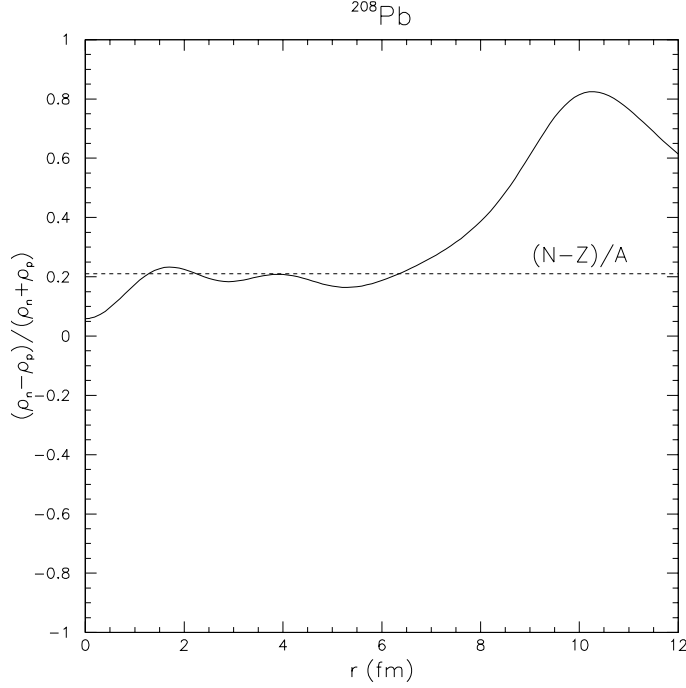
Figure 1: Calculated $(\rho_n - \rho_p)/(\rho_n + \rho_p)$ ratio (full line) compared with the (N-Z)/A ratio (dashed line) for ^{208}Pb. Density distributions are from present HFB calculations.

2 Notations.

Let us first establish the notations used throughout this work (they are the same as those defined in [1, 11, 12]). The mass operator $M_\rho(k, E)$, which is complex and non local, is defined in nuclear matter and calculated in the framework of the Brückner-Hartree-Fock (BHF) approximation, using the Reid hard core interaction [13] as a realistic bare nucleon-nucleon interaction. The central part of the OMP is written as:

$$U_{opt}(\rho, E) = V_0(\rho, E) + \alpha\tau V_1(\rho, E) + i(W_0(\rho, E) + \alpha\tau W_1(\rho, E)), \tag{1}$$

where $\alpha = (\rho_n - \rho_p)/(\rho_n + \rho_p)$ is the asymmetry parameter, τ is +1 for proton and -1 for neutron projectiles, and the potentials V_0, V_1, W_0 and W_1 are the following:

$$V_0(\rho, E) = ReM_\rho^{(0)}(k(E), E), \tag{2}$$

$$V_1(\rho, E) = \frac{\tilde{m}}{m} ReN_\rho(k(E), E), \tag{3}$$

$$W_0(\rho, E) = \frac{m}{\overline{m}} ImM_\rho^{(0)}(k(E), E), \tag{4}$$

$$W_1(\rho, E) = \frac{m}{\overline{m}} ImN_\rho(k(E), E). \tag{5}$$

Note that $k(E)$ denotes the on-energy-shell approximation, so henceforth $M_\rho(E)$ will be a shorter notation for $M_\rho(k(E), E)$. The quantities $\tilde{m}/m$ and $\overline{m}/m$ are, respectively, the k-mass and the E-mass representing the true nonlocality and the true energy dependence of the OMP [14]. Also, according to the prescriptions in [15, 16], the imaginary part of the OMP has been multiplied by the effective mass $\tilde{m}/m$.

For convenience the quantities $ReM_\rho(E)$, $ImM_\rho(E)$, $ReN_\rho(E)$, and $ImN_\rho(E)$ have been parametrised in [1] as sums of $c_{ij}\rho^i E^{j-1}$ terms, for incident nucleon energies ranging from 10 to 160 MeV. Another parametrisation using the same functional form was subsequently published for energies below 10 MeV [17].

In order to get the above nuclear matter results to apply to finite nuclei, the improved local density approximation (LDA)[1] is used:

$$V_{ILDA}(r, E) = (t\sqrt{\pi})^{-3} \int \frac{V_{NM}(\rho(r_1), E)}{\rho(r_1)} \exp(-|\vec{r} - \vec{r'}|^2/t_r^2)\rho(r')d^3r', \qquad (6)$$

where t is the width of the Gaussian used to widen the root mean square radius of the potential, and r_1 is the position at which the interaction is evaluated (r_1 can be taken as r, r', or $(r+r')/2$). Since we know of no convincing theoretical or phenomenological reasons to favor any one of the above prescriptions for the position at which the interaction is evaluated, we arbitrarily chose to use the "middle" one: $(r+r')/2$.
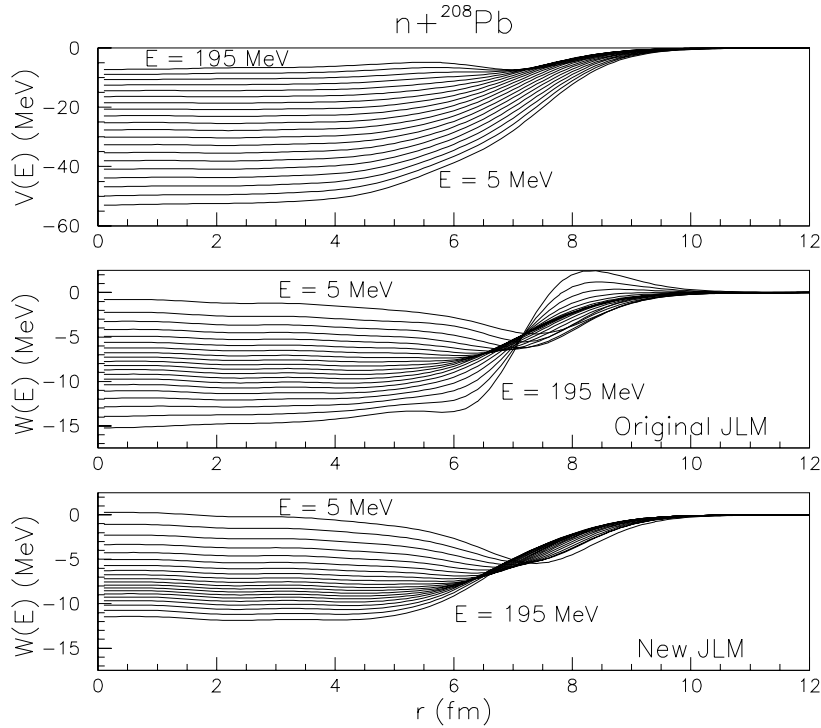

Figure 2: The neutron OMP for ^{208}Pb calculated between 5 and 195 MeV using the JLM model. The real part of the OMP is shown in the upper panel while the middle and lower panels show the imaginary part of the OMP calculated using, respectively, the original JLM parametrisation and our new JLM parametrisation. Density distributions are from present HFB calculations.

3   Nucleon density radial distributions.

In previous studies using the JLM model [5], the nucleon densities are derived from electron scattering experiments. The proton density is extracted from the measured charge density of the nucleus by deconvolution of the proton charge smearing, and the neutron density is taken as the proton density scaled by a N/Z factor. However, microscopic calculations using the Gogny D1S force [18] in the framework of the
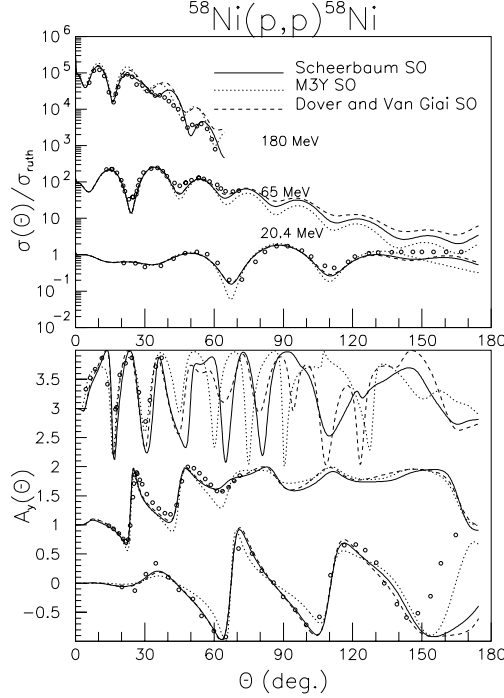
Figure 3: Comparison between the predictions of three prescriptions for evaluation the spin-orbit potential and experimental results for the $^{58}Ni(p,p)^{58}Ni$ reaction at 20.4, 65, and 180 MeV. Full lines denote usage of the Scheerbaum prescription [8], dotted lines denote usage of the M3Y prescription [19], and dashed lines denote usage of the Dover and Van Giai prescription [20]. Note that the differential cross sections at 65(180) MeV are offset by a factor of $10^2(10^4)$, and the polarizations are offset by 1(3).

Hartree-Fock-Bogoliubov method, show that this assumption of a N/Z scaling factor does not hold, as can be seen in Fig. 1 which shows the radial distribution of the asymmetry parameter $\alpha(r)$. It is obvious from Fig. 1 that the microscopic calculation offers a more realistic picture of the nucleon densities to be used in both the calculation of the interaction in nuclear matter and in the improved LDA. So for the rest of this study we will be using microscopic HFB/D1S calculations of the point nucleon densities for our OMP studies.

4   Limitations of the JLM parametrisation.

As we mentioned above, Jeukene, Lejeune and Mahaux fitted their nuclear matter BHF calculations with sums of $c_{ij}\rho^i E^{j-1}$ terms [1]. Thus, the imaginary component of the JLM OMP is parametrised as:

$$Im(M_0(\rho, E)) = \left[1 + \frac{D}{(E - \epsilon_F)^2}\right]^{-1} \sum_{i,j=1}^{4} d_{ij}\rho^i E^{j-1} \tag{7}$$

and

$$Im(N(\rho, E)) = \left[1 + \frac{F}{(E - \epsilon_F)^2}\right]^{-1} \sum_{i,j=1}^{4} f_{ij}\rho^i E^{j-1}, \tag{8}$$

where E is expressed in MeV, ρ in fm^{-3}, and the coefficients d_{ij}, D and f_{ij} are published in [1] for $10 < E < 160$ MeV, and in [17] for $E < 10$ MeV. ϵ_F denotes the Fermi energy which JLM also fitted in
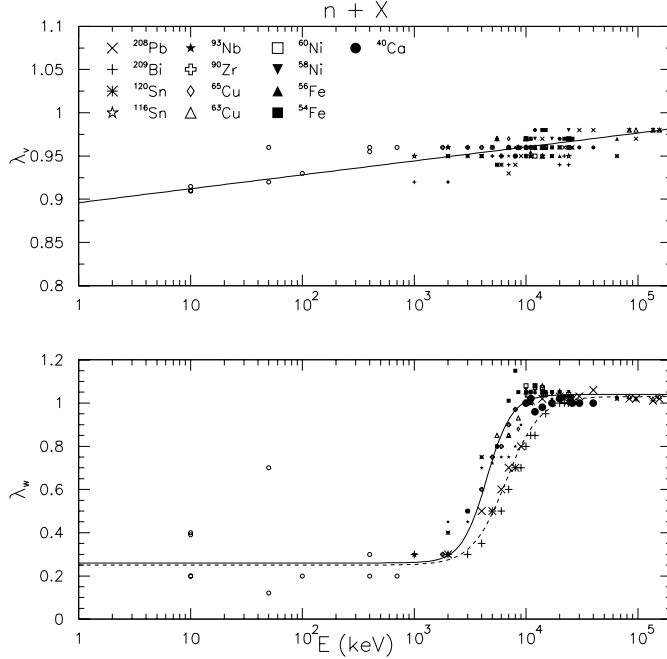
Figure 4: Normalizations for the central part of the neutron OMP. The upper panel shows the normalizations of the real part of the OMP and the lower panel shows the normalizations of the imaginary part of the OMP. The open circles represent the values that give the best fits to the average resonance parameters S_0 and R', and the other symbols represent the values that give the best fits to the differential cross sections and polarizations. The lines are closed forms with parameters fitted to the variations of the normalizations.

[1] ($10 < E < 160$ MeV) and [17] ($E < 10$ MeV). The parametrisations used for the imaginary part of the mass operator exhibit some limitations. First, the parametrisations of $Im(M_0(\rho, E))$ and $Im(N(\rho, E))$ display a discontinuity at 10 MeV, yielding a discontinuity of the volume integral and root mean square radius at 10 MeV. Moreover, the polynomial functional form used for the fits does not lend itself well to extrapolation: if the parameters of [1] are used above 160 MeV the absorption potential becomes emissive, that is clearly an unphysical artifact of the polynomial extrapolation. Figure 2 (middle panel) clearly shows the appearance of an emissive potential above 160 MeV at the surface of the nucleus.

In order to solve the problems above, we have re-fitted the $Im(M_0)$ and $Im(N)$ potentials using the same functional forms, getting new values for the d_{ij}, D and f_{ij} coefficients. For these fits, the value of ϵ_F was taken as:

$$\epsilon_F(\rho, E) = f(E)\epsilon_F{}^l(\rho) + (1 - f(E))\epsilon_F{}^h(\rho), \tag{9}$$

where $\epsilon_F{}^l$ and $\epsilon_F{}^h$ are, respectively, the parametrisations of the Fermi energy in refs. [17] and [1], and $f(E)$ is:

$$f(E) = \frac{1}{1 + exp(\frac{E - E_0}{a_E})}, \tag{10}$$

with $E_0 = 10$ MeV and $a_E = 2$ MeV, so that there is a smooth transition between the low and the high energy behavior of the Fermi energy.

We have put the following constraints on the fits of $Im(M_0)$ and $Im(N)$:
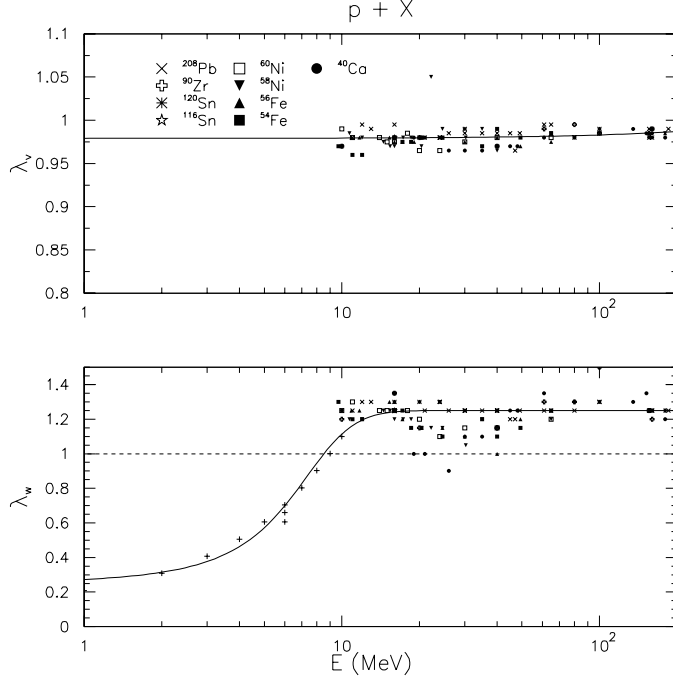
Figure 5: Normalizations for the central part of the proton OMP. The upper panel shows the normalizations of the real part of the OMP and the lower panel shows the normalizations of the imaginary part of the OMP. The crosses represent the values that reproduce the volume integrals of [23], and the other symbols represent the values that give the best fits to the differential cross sections and polarizations. The line represents the parametrisation of the variations of the normalizations.

(i) Between 0 and 10 MeV the target values for $Im(M_0)$ and $Im(N)$ were the values calculated with the low energy parametrisation of Lejeune [17];

(ii) Between 18 and 130 MeV the target values for $Im(M_0)$ and $Im(N)$ were the values calculated with the parametrisation of JLM [1];

(iii) Between 130 and 200 MeV, the target values for $Im(M_0)$ and $Im(N)$ were linearly extrapolated from their respective values at 130 MeV calculated with the JLM parametrisation [1].

It is important to note that the region between 9 and 19 MeV was left free of constraints so that the function could "heal" at the discontinuity. The fit was performed on 2500 points in (ρ, E) space, with 50 values of ρ ranging from 2×10^{-9} to 2×10^{-1} fm^{-3} and 50 values of E ranging from 0.1 MeV to 200 MeV.

This new parametrisation no longer exhibits a discontinuity at 10 MeV, and the lower panel of Fig. 2 shows that the absorption part of the potential is now no longer positive above 150 MeV.

Fig. 2 shows the neutron on ^{208}Pb potential between 5 and 195 MeV, as calculated with the JLM OMP. As it can be seen, the real potential (upper panel) goes from a volume potential at 5 MeV to a surface peaked potential at 195 MeV, this transition taking place around 160 MeV. The imaginary optical potential (lower panel) on the other hand exhibits a transition from surface peaked at 5 MeV to volume shaped at 195 MeV. This transition occurs at about 40 MeV. More importantly, the imaginary potential evaluated with our new parametrisation is no longer emissive.
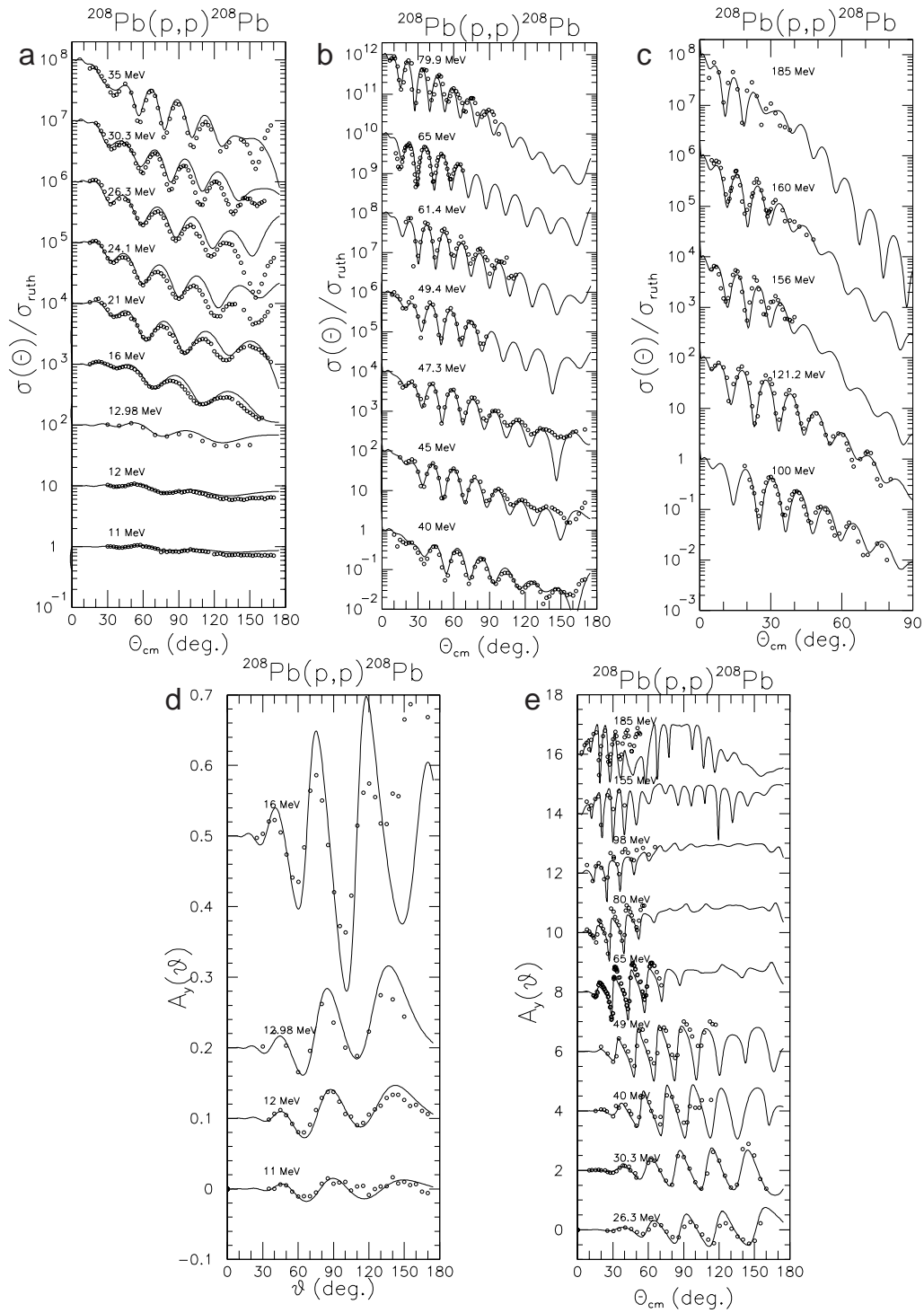
Figure 6: Comparison between calculated and measured differential cross sections (a, b, and c) and analyzing powers (d and e), for protons incident on ^{208}Pb between 11 and 185 MeV.
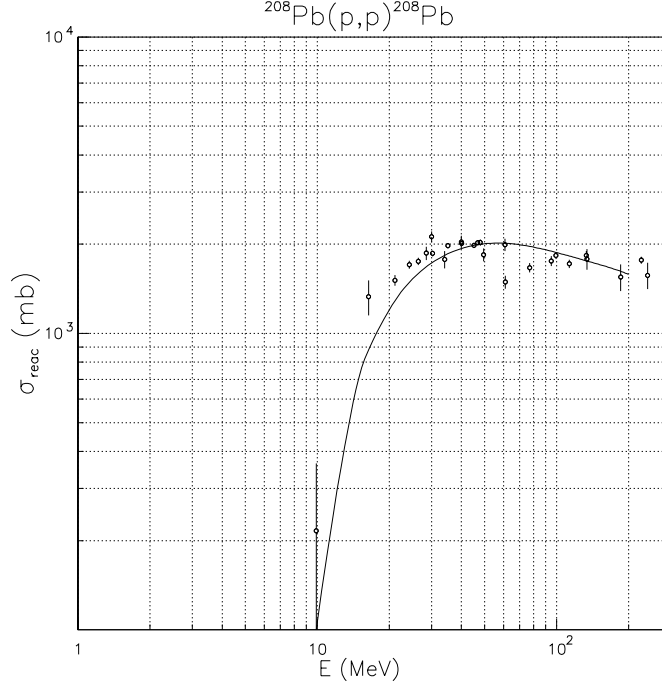
Figure 7: Comparison between calculated and measured reaction cross sections, for protons incident on ^{208}Pb.

5   Spin-orbit potential.

In order to faithfully reproduce experimental polarizations, one needs not only a good central potential, but a good spin-orbit potential as well. However, the nuclear matter approach of JLM is not applicable in the case of a spin-orbit interaction since a SO interaction involves a derivative in position space; thus another prescription for the calculation of the SO potential is necessary. Moreover, if this SO potential is to be used above 100 MeV, it must be complex in order to account for experimental results. Since the M3Y [19] potential used in several published studies [5, 6, 7] is real, it cannot be expected to work up to 200 MeV. We have evaluated two alternatives prescriptions: the Scheerbaum SO form factor (Eq. 11) [8] and the Dover and Van Giai SO form factor (Eq. 12) [20]

$$U_{n(p)}^{so}(r) = \frac{1}{r}\frac{d}{dr}\left(\frac{2}{3}\rho_{p(n)} + \frac{1}{3}\rho_{n(p)}\right), \tag{11}$$

and

$$U_{so}(r) = (1 + \alpha\rho(r))^{-1}\frac{1}{r}\frac{d\rho}{dr}, \tag{12}$$

where $\rho_{n(p)}$ is the neutron (proton) radial density, $\rho = \rho_n + \rho_p$, and $\alpha = 4.89$ fm^3. Note that the Scheerbaum prescription yields different SO form factor for neutrons and protons. In order to get a spin orbit potential, the above form factors have to be multiplied by phenomenological normalizations of the SO potential depths, $\lambda_{v_{so}}$ and $\lambda_{w_{so}}$:

$$V_{n(p)}^{so}(r) = \lambda_{v_{so}}U_{n(p)}^{so}(r), \tag{13}$$

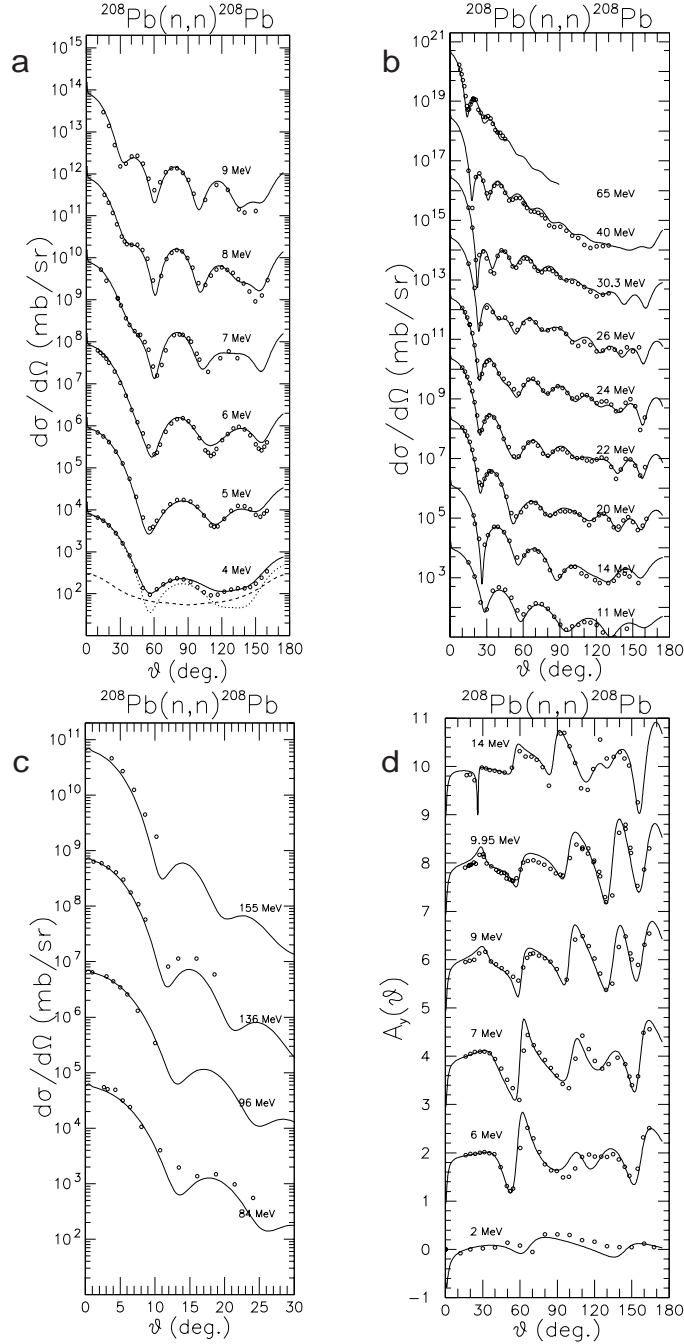$$W_{n(p)}^{so}(r) = \lambda_{w_{so}}U_{n(p)}^{so}(r). \tag{14}$$

Figure 8: Comparison between calculated and measured differential cross sections (a, b, c), and analyzing power (d), for neutrons incident on ^{208}Pb between 4 and 155 MeV. The full line represent the total elastic cross section, the dashed line represents the compound elastic cross section, and the dotted line represents the direct elastic cross section.

We performed a systematic comparison of angular distributions predicted by the three prescription for the SO potential (M3Y, Dover and Van Giai, Scheerbaum). The Scheerbaum prescription gives an overall
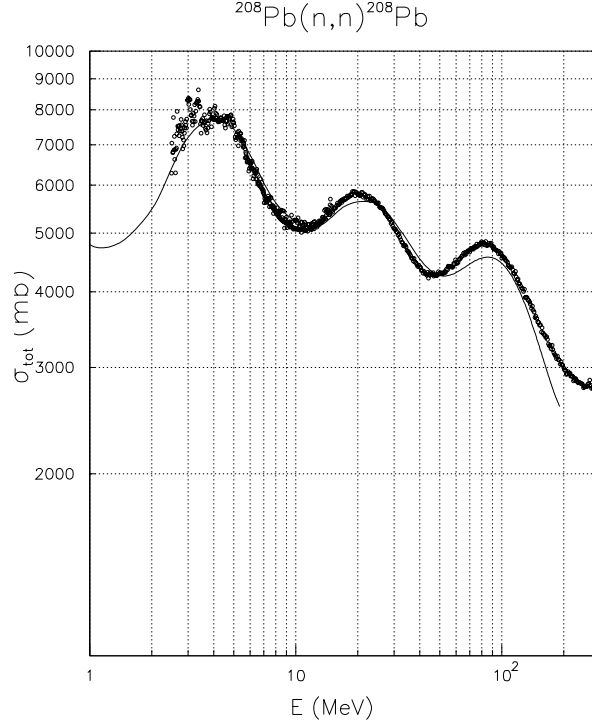
Figure 9: Comparison between calculated and measured total cross sections, for neutrons incident on ^{208}Pb.

better agreement with the experimental data, especially at high energies. Fig. 3 shows an example of such a comparison in the case of $p +^{58} Ni$ at 20.4, 65 and 180 MeV. While at lower energies all three prescriptions yield satisfactory fits, at 180 MeV the prediction using the Scheerbaum prescription is closer to experimental data than the other two predictions.

6   Phenomenological normalization parameters.

In the full OMP, eq. 15, several phenomenological potential depth normalizations are present. Also, note in Eq. 15 the presence of a Coulomb Spin-Orbit term (or Mott Schwinger potential) [21, 22]

$$U(r) = \lambda_v (V_0(r) + \alpha V_1(r)) + i\lambda_w (W_0(r) + \alpha W_1(r))$$

$$+\frac{\hbar^2}{2m^2c^2}\vec{\ell}.\vec{\sigma}(\lambda_{v_{so}} V_{so}(r) + i\lambda_{w_{so}} W_{so}(r))$$

$$+V_c(r)$$

$$+\frac{\hbar^2}{2m^2c^2}(\mu - a)\vec{\ell}.\vec{\sigma}\frac{1}{r}\frac{d}{dr}V_c(r), \tag{15}$$

where $a = 0$ for neutrons and $a = 1/2$ for protons.

In the central part of the OMP, λ_v and λ_w are the potential depth normalizations of the real and imaginary parts of the OMP, respectively. Previous studies have shown these normalizations to be close to unity [6, 3], illustrating that λ_v and λ_w carry only fine tuning information for the microscopic central OMP. On the other hand , in the SO part of the potential, all the energy dependence of the SO potential is carried in the phenomenological normalizations of the potential depths $\lambda_{v_{so}}$ and $\lambda_{w_{so}}$.

In order to determine the values of the potential depth normalizations, we allowed them to vary freely while fitting over 500 individual angular distributions (differential cross sections and analyzing powers). For central potentials, λ_v and λ_w exhibit some common features. For both neutron (Fig. 4) and proton (Fig. 5) projectiles the λ_v's are quite constant around 0.96. The λ_w's for the neutron (Fig. 4) and proton (Fig. 5) potentials exhibit a plateau for energies in excess of 10-15 MeV, and a sharp decline below, down to about 0.25 at 1 MeV. There are however some differences, the most striking being that the plateau above 10 MeV lies at $\lambda_w = 1.05$ for neutrons and at $\lambda_w = 1.25$ for protons. Another strong difference is the fact that the neutron normalizations are different depending on whether the target is doubly-magic or not, while the proton normalizations do not exhibit such differences. This interesting effect of nuclear structure on scattering can be seen only at lower energies ($E \leq 15$ MeV).

The normalizations of the spin-orbit potential for neutrons and protons are identical. The depth of the real part of the spin-orbit potential is exponentially decreasing, while the imaginary part decreases linearly, crossing zero at 20 MeV. We have then expressed the energy variations of the potential depth normalizations with functional forms, thus getting the global OMPs (one OMP for neutrons and one for protons) that are going to be used in the next section.

7   Comparison with experimental data.

In this section we show a comparison between experimental data for ^{208}Pb and predictions from our global JLM OMP. Other comparisons are available on request.

Differential cross sections for (p,p) scattering on ^{208}Pb are displayed in Figs. 6 a, b and c. The agreement between measurements and calculations is generally good across the whole energy range. At low energies, the differential cross sections exhibit a strong damping of their oscillations due to the proximity of the Coulomb barrier. At energies between 16 MeV and 30 MeV the model seems to overestimate the elastic cross section at the back angles. At higher energies the experimental elastic cross section are fairly well accounted for by the calculations up to E=185 MeV. The analyzing powers (Figs. 6d and e) are also well reproduced by the model which also reproduces the damping exhibited by the polarizations at low energy. The reaction cross section (Fig. 7) is equally well reproduced at energies ranging from below the Coulomb barrier (10 MeV) to 200 MeV. For neutrons incident on ^{208}Pb, the comparison between experimental and calculated elastic differential cross section shows good agreement from E = 4 MeV to 155 MeV (Figs. 8 a, b and c). At the lower energies (4 to 10 MeV), the compound and direct components of the elastic cross section are of comparable influence and must both be included in the calculations in order to reproduce the experiments. At the higher energies (84 to 155 MeV, Fig. 8c) the fit is not so good, probably due to a poor energy resolution which allows for contamination by inelastic scattering. The polarizations (Fig. 8d) are also accounted for by the model. The total cross section (Fig. 9) is reproduced with less than 5% of error between E=3 MeV and 150 MeV, beyond which the error increases to 10%.

In the case of other spherical nuclei (i.e., ^{40}Ca, ^{90}Zr, ^{93}Nb, ^{116}Sn, ^{120}Sn, ^{208}Pb, ^{209}Bi) or quasi-spherical nuclei (i.e., ^{54}Fe, ^{56}Fe, ^{58}Ni, ^{60}Ni, ^{63}Cu, ^{65}Cu) the agreement between the new JLM model predictions and experimental data is comparable with that obtained for ^{208}Pb.

To summarize, we have found that the agreement between our calculations and experimental data was generally very good. However, some problems do remain : for instance, for incident protons in the energy region ranging from 20 to 40 MeV, the best fit λ_w values are substantially lower (by about 10-20%) than the parametrised λ_w; resulting in some overestimation of the differential cross section at back angles. In the case of a neutron projectile, the total cross section exhibits two problems: in the 15 to 30 MeV region the total cross section is often overestimated by as much as 10%, and above 150 MeV the predicted total cross section can be up to 10% lower than the experimental cross section. That high energy mismatch of the total cross sections might be explained by the absence of the pion creation channels in the model. Nevertheless, the overall agreement of our calculations with experimental data can be considered to be very satisfactory, especially considering the fact that the calculations are performed using one set of parametrisations that is global and not specifically geared to reproducing ^{208}Pb experimental results.

8   Conclusions.

In this work we build an OMP that fixes the limitations of the original microscopic JLM OMP. By re-fitting the imaginary central potential over a wider energy range and by systematically studying the variations of the free parameters of the potential, we have constructed an OMP that predicts fairly accurately the integrated and differential cross sections of nucleons incident on spherical or quasi-spherical nuclei. Moreover, by using the Scheerbaum prescription for the spin-orbit potential, the quality of the fit to experimental observables was noticeably improved. Keeping in mind its energy (0-200 MeV) and target deformation limitations (spherical or quasi-spherical nuclei), our JLM global OMP is useful to account for experimental data over a wide range of projectile energy and targets with good accuracy, making it suitable for use as a global potential for analyzing experimental data and in nuclear physics applications.

References

[1] J.P. Jeukenne, A. Lejeune, and C. Mahaux, Phys. Rev. **C16**, 80 (1977).

[2] F.A. Brieva, and J.R. Rook, Nucl. Phys. **A291**, 299 (1977).

[3] Ch. Lagrange and J.C. Brient, J. Phys. (Paris) **44**, 27 (1983).

[4] A. Lejeune, and P.E. Hodgson, Nucl. Phys. **A295**, 301 (1978).

[5] J.S. Petler, M.S. Islam, R.W. Finlay, and F.S. Dietrich, Phys. Rev. **C32**, 673 (1985).

[6] S. Mellema, R.W. Finlay, F.S. Dietrich and F. Petrovich, Phys. Rev. Lett. **51**, 1629 (1983).

[7] L.F. Hansen, F.S. Dietrich, B.A. Pohl, C.H. Poppe, C. Wong, Phys. Rev. **C31**, 111 (1985).

[8] R.R. Scheerbaum, Nucl. Phys. **A257**, 77 (1976).

[9] F.S. Dietrich, private communication.

[10] J. Raynal, private communication.

[11] J.P. Jeukenne, A. Lejeune, and C. Mahaux, Phys. Rev. **C14**, 1391 (1974).

[12] J.P. Jeukenne, A. Lejeune, and C. Mahaux, Phys. Rev. **C15**, 10 (1977).

[13] R.V. Reid, Ann. Phys. (NY) **50**, 525 (1972).

[14] J.P. Jeukenne, A. Lejeune, and C. Mahaux, Phys. Rep. **25C**, 83 (1976).

[15] J.W. Negele and K. Yazaki, Phys. Rev. Lett. **47**, 71 (1981).

[16] S. Fantoni, B.L. Friedman, and V.R. Pandharipande, Phys. Lett. **104B**, 89 (1981).

[17] A. Lejeune, Phys. Rev. **C21**, 1107 (1980).

[18] J.F. Berger, M. Girod, and D. Gogny, Comp. Phys. Comm. **63**, 365 (1990).

[19] G. Bertch, J. Boryowicz, H. McManus and W.G. Love, Nucl. Phys. **A284**, 399 (1977).

[20] C.B. Dover and N. Van Giai, Nucl. Phys. **A190**, 373 (1972).

[21] J. Schwinger, Phys. Rev. **73**, 407 (1948).

[22] W. Heckrotte, Phys. Rev. **101**, 1406 (1956).

[23] Y. Wang, C.C. Foster, R.D. Polak, J. Rapaport and E.J. Stephenson, Phys. Rev. **C47**, 2677 (1993).